Melt Pool Imaging using a Configurable Architecture Additive Testbed System

Joseph N. Zalameda*, Samuel J. A. Hocker, Joshua M. Fody and Wesley A. Tayon

NASA Langley Research Center Hampton, VA 23681-2199

ABSTRACT

This paper describes the inline (coaxial to laser) near infrared (NIR) camera sensor on the Configurable Architecture Additive Testbed (CAAT). The CAAT is an instrument that provides the capability to investigate laser based additive manufacturing (AM) processes and is configured for the metal powder bed fusion process. A low cost NIR camera is radiometrically calibrated to obtain coaxial, inline, imagery of laser generated melt pools. The camera capabilities, system optical path, and the uncertainty in the temperature measurement from NIR surface area scans on a bare titanium alloy plate are presented and discussed. The surface radiance measurements are compared to optical microscopy images of the melt pool width and depth. A metallic additive manufacturing process thermal model is developed in order to predict thermal distributions during laser scanning. The predicted thermal distributions by the model for different configurations are compared to the coaxial NIR measurements and discussed.

Keywords: Additive manufacturing, melt pool imaging, in-situ monitoring, coaxial near infrared camera, optical microscopy, finite element model

1. INTRODUCTION

This paper describes the inline (coaxial to laser) near infrared (NIR) camera sensor on a Configurable Architecture Additive Testbed (CAAT). The CAAT system is a configurable architecture system specifically developed to test process parameters, test in-situ sensors, and validate model predication tools. The CAAT system is comprised of an enclosed environmental chamber, build platform, and multiple view port windows. The CAAT system is used for metals manufacturing research using a Laser Powder Bed Fusion (LPBF) method. LPBF is a common additive manufacturing technique for rapid prototyping metals manufacturing [1]. A major area of importance is the integrity and repeatability of the LPBF additive manufactured part and in-situ nondestructive evaluation (NDE) sensors can contribute a critical role for build assessment [2-3]. In the CAAT system, a high-power focused laser is scanned over a bed of metal powder, layer by layer, to melt the powder at precise locations and thus produce near net shaped parts. The architecture of the CAAT system is designed for the addition of various sensors. The NIR camera sensor investigated uses a single camera and is less complex as compared to other sensors developed using dual camera pyrometer imaging systems [4] for melt pool imaging. The simplicity of a single camera system provides an easier path for integration onto commercial additive manufacturing systems, however there are limitations that will be discussed in this paper.

The NIR camera investigated is positioned in line with the laser to obtain high spatial resolution. The in-line NIR camera is calibrated to obtain imagery of the metal melt pool and semi-solid regions. A blackbody calibration technique is described in this paper and was necessary to help determine the melt pool radiance field [2]. The radiance calibration will help to identify the transition points between solidus and liquidous regimes for the melt pool. Ex-situ optical microscopy measurements of the melt pool width and depth are also used for a comparison to the NIR imagery. Melt pool features are understood to have a strong correlation with microstructural defects [2]. Observable features of interest include cooling gradients, melt area width, and shape.

*joseph.n.zalameda@nasa.gov; phone 1 757-864-4793; fax 1 757-864-4914; http://nde.larc.nasa.gov

The radiance imagery are compared to modeling results. The three-dimensional finite element model is developed to predict transient temperature distribution and history for single scan lines at various process parameter settings. The model accounts for solid and liquid heat diffusion, melting/evaporation phase change, and radiant/convective losses. This model is under development primarily to guide process parameter selection and to understand the sensitivity of part performance variation to differences in process variables. Minimizing model processing speed is therefore a priority. Consequently, complex phenomenon within the melt pool are approximated by implementing a volumetric heat source model and automating the selection of heat source parameter settings which produce melt pool dimensions closest to observed. Calibrated thermal models can be validated and help to determine processing parameters for optimal melt pool dimensions.

2. ADDITIVE MANUFACTURING AND MEASUREMENT SYSTEM DESCRIPTION

2.1 Configurable Architecture Additive Testbed (CAAT)

The CAAT system is comprised of an enclosed environmental chamber which has been modified to conduct LPBF experiments with a variety sensors and multiple view port windows for various camera configurations as shown in Figures 1a and 1b. The environmental chamber is fitted with a variety of sensors such as Oxygen (< 10 ppm operation), humidity sensors, and thermocouples. The laser source was an IPG Model YLR-1000-WC-Y14, with a modulated continuous emission wavelength of 1070 nm and a maximum power of 1 kW. The scan system was a SCANLAB GmbH IntelliSCAN III 20 with a LINOS F-Theta-Ronar lens with a 255 mm focal length.

The in-line (coaxial to the laser heat source) camera sensor setup is shown in Figure 2. The camera field of view follows the laser path using the SCANLAB GmbH camera adapter that consists of a focusing objective and a beam splitter. This coaxial method is used to obtain the highest resolution imagery of the melt process. The beam splitter in the camera adapter separates the 1070 nm laser beam from the visible and NIR wavelengths that are measured by the camera.

The in-line camera used is a low cost Basler acA640-750um camera. This camera has an ON Semiconductor CMOS sensor, 4.8 x 4.8 um pixel pitch, 640 x 480 pixel array, selectable dynamic range between 8 and 10 bits, and maximum frame rate of 751 Hz. The spectral sensitivity of the sensor is shown in Figure 3. As shown in Figure 3 the sensor's relative response at 900 nm is approximately 30 percent and at 1000 nm is approximately 10 percent. Thus the sensor is adequate for NIR measurements. The camera's optical path was configured with a 880 nm narrow band filter with a bandwidth of 875 to 884 nm. This narrow band was selected to reduce signal saturation due to the camera's limited dynamic range and further reduce the potential of laser reflections from damaging the detector. A drawback however is the reduced sensitivity to lower temperatures. This will be discussed in the following calibration section.

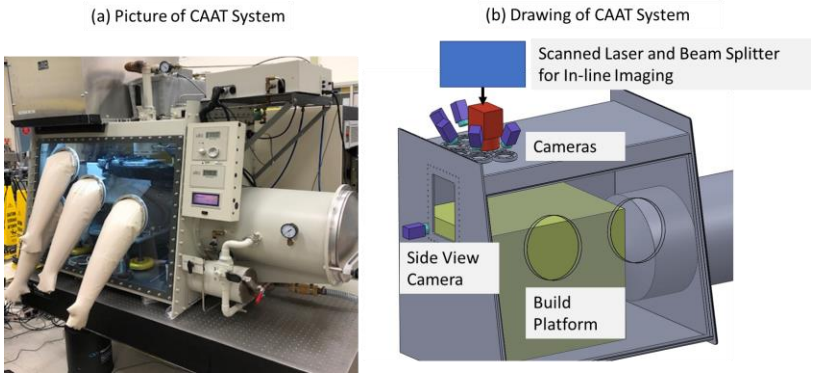

Figure 1: CAAT system setup (a) picture of system and (b) drawing of test setup.

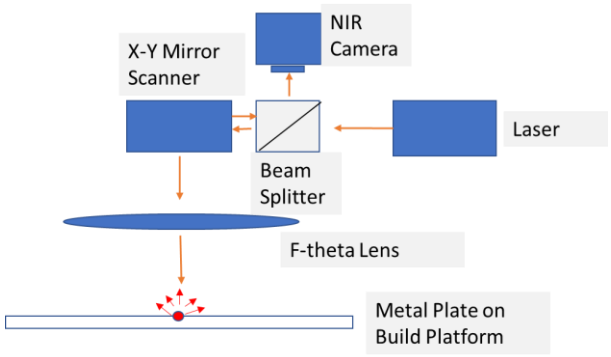

Figure 2: In-line NIR camera setup.

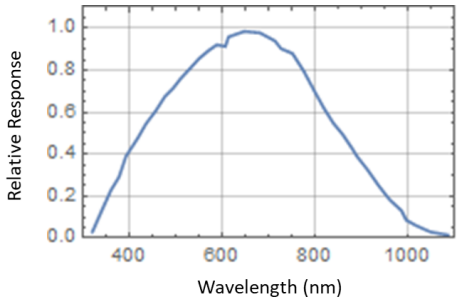

Figure 3: In-line camera sensor relative response.

2.2 Calibration of NIR Camera Sensor

The coaxial NIR camera was calibrated to obtain radiometric imagery of the metal melt pool. A blackbody calibration technique is described in this paper and was necessary to calibrate the pixel intensity counts to radiance. The in-line NIR camera was configured with the barrel optic and CAAT beam splitter. These items were removed from the CAAT system to allow a direct view of the blackbody radiation source. The setup is shown in Figure 4. The blackbody radiation source (Mikron M335) was varied in temperature between 900 to 1500 degrees Centigrade. For each temperature, the integration time was varied at the following values: 59, 75, 100, 150, 300, 500, 700, 900, and 1,500 microseconds and an averaged pixel intensity counts was obtained from the image center.

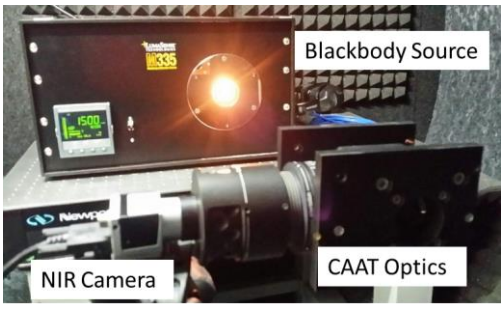

Figure 4: In-line camera sensor calibration setup

The effective radiance measured from the blackbody source to the camera's sensor is determined using equation 1 which is Planck's blackbody radiation equation. The in-band radiance is defined by the filter used and is 875 to 884 nanometers. The filter response is estimated to be a top hat function with 95 percent transmission over the bandpass. The sensor's

response is taken into account in equation (1) by linear interpolation of the sensor's relative response over the wavelength band. The objective optics and scanning mirrors are not taken into account and are presumed to be spectrally flat over the wavelength band.

$$Radiance = \int_{\lambda_1}^{\lambda_2} \frac{c_1}{\lambda^5 \left(e^{\frac{c_2}{\lambda (T+273.15))}}\right)} * sensor(\lambda) * filter(\lambda) * d\lambda \quad \text{where } c_1 = 2 * h * c^2 \quad \text{and} \quad c_2 = \frac{h * c}{k} \tag{1}$$

For equation (1), λ is the wavelength variable, λ_1 and λ_2 are the wavelength bounds of 875 to 884 nanometers respectively, and T is temperature in degrees Celsius. The constants c_1 and c_2 are a function of the speed of light (c = 2.99792 x 10^{17} nanometers/second), Plank's constant (h = 6.26 x 10^{-16} nanometers^2 Kg/second), and Boltzmann's constant (k = 1.3806 x 10^{-5} nanometers^2 Kg/second^2//Kelvin). From equation (1) the radiance versus the blackbody temperature is calculated over a range of 900 to 1900 degrees Celsius as shown in Figure 5, and therefore for each intensity versus integration time curve in Figure 6(a), the radiance is known. Shown in Figure 6(b) is the count rate (pixel intensity over integration time

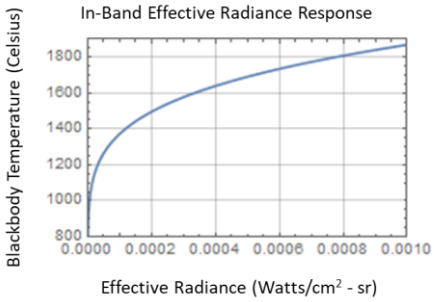

Figure 5: The in-band effective radiance response of the CAAT optical path and sensor.

obtained from Figure 6(a)) versus the effective radiance. As expected the response is highly linear with an R squared value of 0.9931 for the given equation: Effective Radiance = 5.5479x10^{-6} + 0.00104351* ((counts – dark value)/integration time). The dark value, measured with the lens covered, was on average around 0.5 counts and was corrected accordingly for the camera gain setting. For a given integration time and camera pixel counts (dark offset counts subtracted), the camera imagery can then be converted to effective radiance imagery. Shown in Figure 7 are the pixel intensity counts for a given blackbody temperature at an integration time of 100 us. As can be seen in this graph, for lower temperatures (less than 1,000 degrees Celsius), the variation in the counts is very small over a large temperature variation. For this range of temperatures the camera noise can produce relatively large errors in the radiance as compared to higher temperatures. As shown in Figure 7, for higher temperatures (greater than 1100 degree Celsius), the camera noise effect is much less since the pixel values are greater over the higher temperature range and this will cause smaller errors in the radiance. For example, if the pixel count error is +/- 1 count (8 bit acquisition and integration time of 100 us) then at 900 degrees Celsius the approximate error is +/- 65 and at 1500 degrees Celsius the approximate error is +/- 6 degrees.

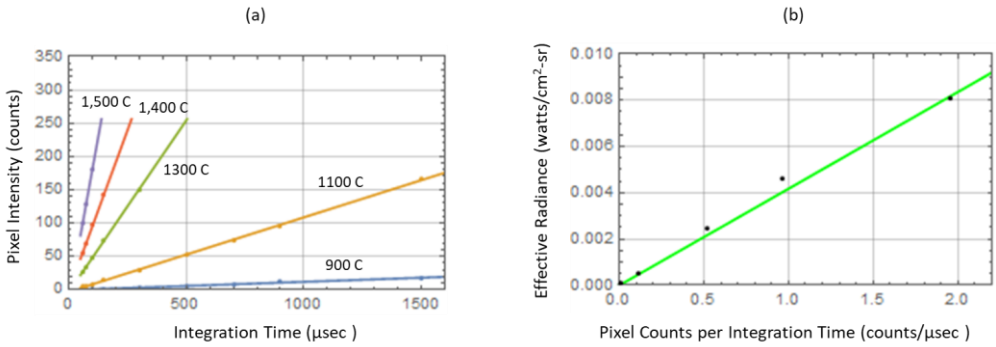

Figure 6: In-line camera sensor blackbody calibration results with conversion to effective radiance.

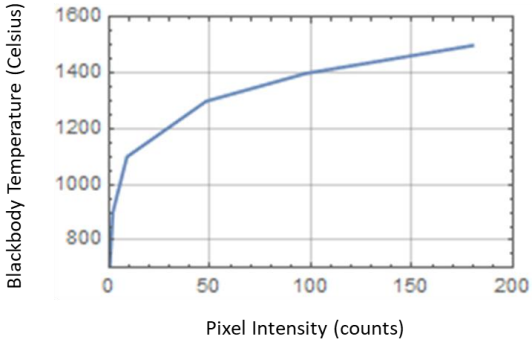

Figure 7: Camera sensor response at 100 us integration time as a function of blackbody temperature.

3. MEASUREMENT RESULTS

3.1 Melt Pool Imaging of Ti-6Al-4V Plate

The in-line NIR camera was used to obtain imagery of the metal melt pool on a Ti-6Al-4V plate. The test plate photograph is shown in Figure 8. The solid plate is approximately 2.5 cm in width by 12.7 cm in length with a thickness of 2.5 mm. Various laser scan tracks of power and scanning velocities were used to generate melting at the surface.

Figure 8: Photograph of Ti-6Al-4V test plate used for CAAT testing.

Shown in Figure 9 are example laser generated melt pool images of the Ti-6Al-4V metal plate. The laser heating power of 280 Watts and laser scanning speeds of 500, 850, and 1200 mm/second were used. The images were selected in the middle of the laser scan path to insure the laser scanning speed is constant and the thermal profiles have reached steady state. The images were obtained at a frame rate of approximately 2,000 kHz with pixel array dimensions of 144 x 144, 8 bit dynamic range, and with a camera integration time of 100 us. The pixel resolution using a calibrated target was determined to be approximately 11 microns/pixel and therefore the image field of view is 1.6 x 1.6 mm^2. Also shown in Figure 9 are a comparison of the vertical line plots over the center of the melt pools for the various laser scanning velocities. As expected, the faster the laser scanning speed the energy delivered per mm is lower. The laser power was constant at 280 Watts and therefore the energies delivered for velocities of 500, 850, and 1200 mm/second were 0.23, 0.33 and 0.56 Joules/mm respectively.

3.2 Melt Pool Imaging Comparison to Optical Microscopy

The calibration as discussed in section 2.2 was used to obtain radiometric imagery of the metal melt pool. The pixel intensity counts are converted to effective radiance. The data was collected for various gain values ranging from 0 to 10 dB. The gain was corrected by adjusting the slope of the radiance calibration curve accordingly. Shown in Figures 10-12 are the converted images to effective radiance images for different scan speeds. Also shown in Figures 10-12, are the comparison of the radiance imagery to cross sectional optical microscopy measurements of the melt pool width and depth.

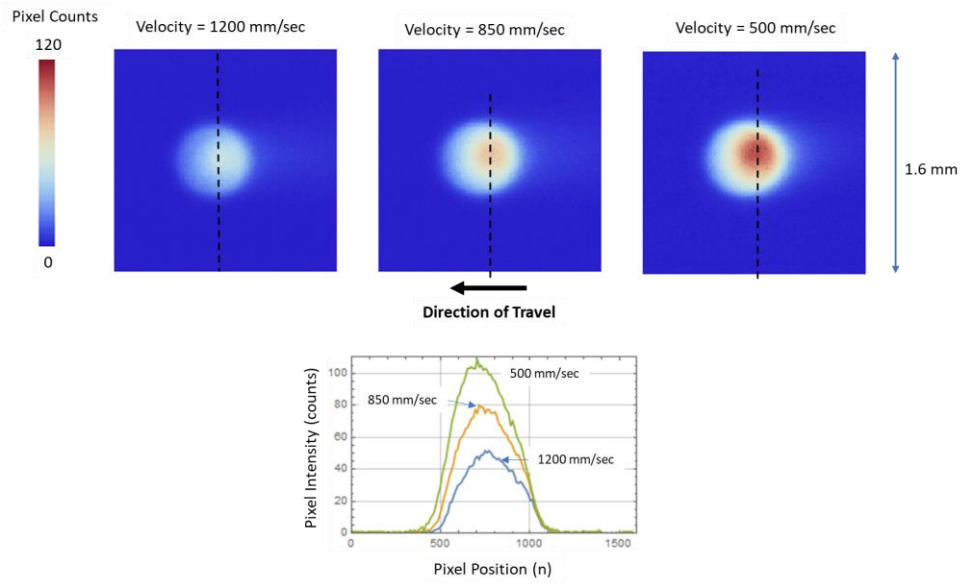

Figure 9: Camera melt pool imaging at 100 us integration time for various laser scan velocities with corresponding vertical line plots over the melt pool center.

Ex-situ optical microscopy was used to measure the width and depth of the melted zone in the middle of each scan track. The optical microscopy images were obtained on an inverted optical microscope at a magnification of 500x. Each track was sectioned approximately in the middle of the scan track. Prior to imaging, samples were mechanically polished and etched with Kroll's reagent (93 mL distilled water, 6 mL HNO3, 1 mL HF) to reveal the underlying microstructure. For the depth measurements, the original top surface of the plate was used as reference point and depth was measured off this location. The measurement errors are estimated to be +/- 3 microns. From the optical microscopy measurements, the melt pool widths for the scanning velocities of 1200, 850, and 500 mm/second are 14, 16, and 23 pixels respectively. These widths are fitted to the cross sectional radiance curves as shown in Figures 10, 11, and 12. As can be seen, the melt pool widths and depths are larger for slower laser scanning speeds.

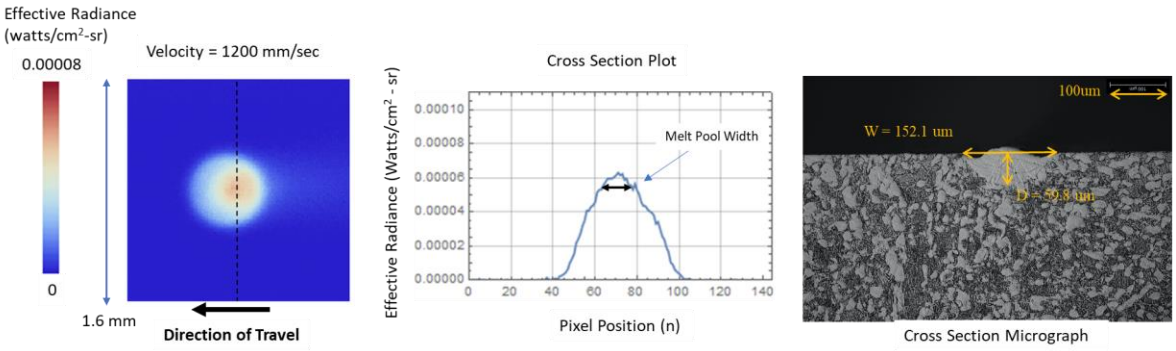

Figure 10: Conversion to radiance image for the 1200 mm/second laser scanning speed with comparison to optical microscopy measurement of the melt pool width and depth.

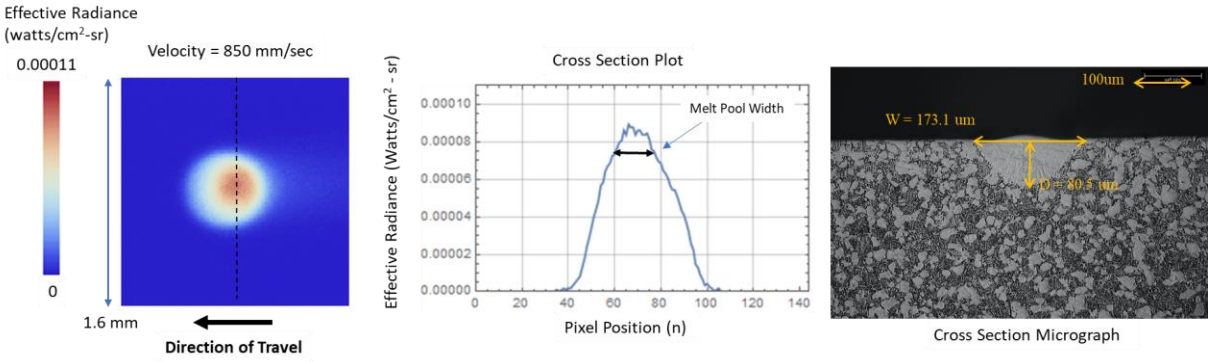

Figure 11: Conversion to radiance image for the 850 mm/second laser scanning speed with comparison to optical microscopy measurement of the melt pool width and depth.

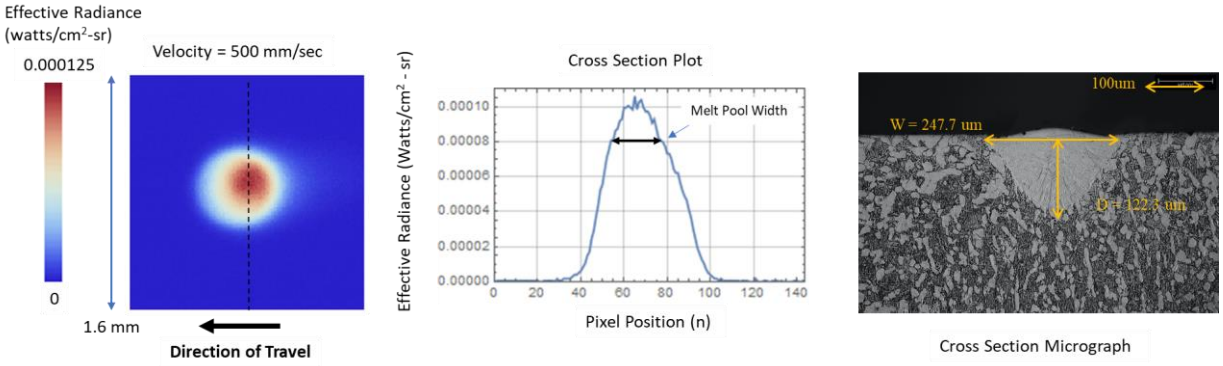

Figure 12: Conversion to radiance image for the 500 mm/second laser scanning speed with comparison to optical microscopy measurement of the melt pool width and depth.

4. ESTIMATION OF EMISSIVTY AND MELT POOL WIDTH MODELING RESULTS

4.1 Estimation of Emissivity

From the optical microscopy results of the melt pool width, an estimation of the emissivity can be obtained by relating the known melt pool width with the radiance images by converting the radiance values to temperature at the boundary. The temperature as a function of radiance is determined from equation 1 for the spectral imaging band of the optical system used. The effective radiance values can then be converted to temperature by dividing by emissivity. The apparent emissivity is estimated at the boundary where the melt pool is confined. The solidus point of Ti-6Al-4V is found from the literature to be at approximately 1605 degrees Celsius [6]. The melt pool width from the optical measurement can then be converted to the pixel width given the image resolution of 11 microns/pixel. The melt pool width from the optical microscopy measurements is used to adjust the emissivity to match the melting point of Ti-6Al-4V at the melt pool boundary within the thermal image. The apparent emissivity is estimated for all three of the laser scanning velocities. It important to note that the emissivity within the melt pool is not known, since at temperatures past the melting point, the emissivity can vary significantly.

The melt pool widths for the scanning velocities of 1200, 850, and 500 mm/second are 14, 16, and 23 pixels respectively from the optical microscopy measurements. These results are summarized in Table 1. These widths are fitted to the cross sectional radiance curves shown in Figures 10-12. The effective radiance is the determined from the plots to be 8.1×10^{-5}, 7.4×10^{-5}, and 5.2×10^{-5} for the 500, 850, and 1200 mm/second velocities respectively. Converting these radiance values to temperature of 1605 degree Celsius yielded emissivity values of 0.15, 0.22, and 0.24 for the 1200, 850, and 500 mm/second

velocities respectively. The average taken from these emissivity values was 0.20 +/-0.047. The apparent variation in the emissivity was unexpected for the solidus Ti-6Al-4V at 1605 degrees Celsius and are different than previously reported values with emissivity values greater than 0.2 @ 1,000 degrees Celsius and trending upward for increasing temperature [7]. The observed variation may be explained by a combination of surface geometry effects at the area of laser melting, reflection of laser detected by the camera, and blurring effects due to the camera integration time versus scanning velocity. For example, as shown in Figure 10, the surface geometry of the 1200 mm/sec laser scanning speed optical microscopy image shows significant surface variation at the edges of the melt pool as compared to the other optical microscopy images. This geometric effect could have influenced the detected radiance and resulted in a lower apparent emissivity. The trend of the emissivity increasing with rising input power was noted. Shown in Figure 13 are the thermal contour plots of the melt pool shape and size as calibrated from the optical microscopy measurements. As the laser scanning speed increases the amount of energy delivered per length is reduced thus producing a smaller melt pool.

Table 1. Estimation of Emissivity at Solidus Boundary from Optical Measurements.

Laser Scanning Speed (mm/sec)	Melt Pool Width Optical Microscopy (Microns)	Melt Pool Thermal Image Width (Pixels)	Thermal Radiance Value (Watts/cm² – sr)	Emissivity Value @ 1604 Degrees Celsius
1200	152 +/- 3	14 +/- 1	$5.2 \times 10^{-5} +/- 0.04 \times 10^{-5}$	0.15 +/- 0.005
850	173 +/- 3	16 +/- 1	$7.4 \times 10^{-5} +/- 0.04 \times 10^{-5}$	0.22 +/- 0.005
500	248 +/- 3	23 +/- 1	$8.1 \times 10^{-5} +/- 0.04 \times 10^{-5}$	0.24 +/- 0.005

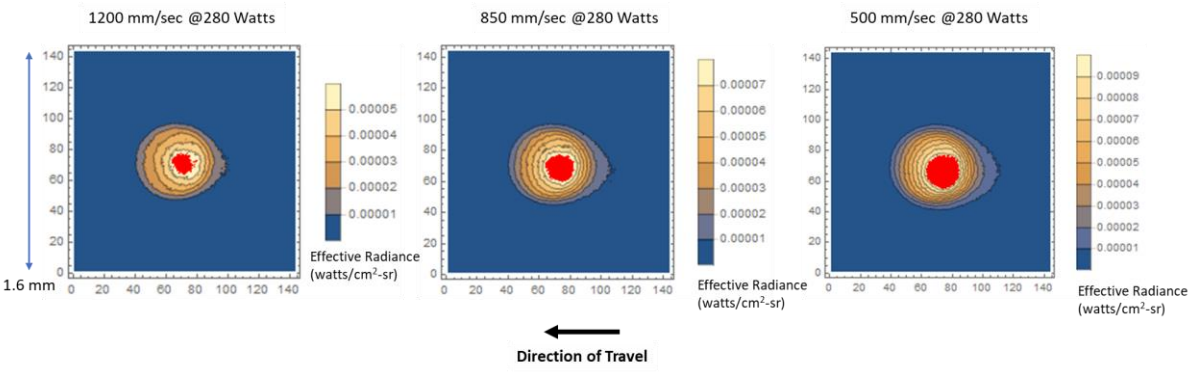

Figure 13: Thermal contour images of the melt pool versus laser scanning velocity.

4.2 Preliminary Melt Pool Model Results

A single scan track thermal model for the metallic LPBF process has been developed and is being integrated within a novel calibration paradigm. The finite element analysis (FEA) thermal model was developed using COMSOL Multiphysics® software [8] and employs a volumetric heat source model, based on a simplification of the well-known Goldak double ellipsoid [9], to reduce simulation time. The FEA thermal model employs a hexahedral geometry with a 25 degree Celsius ambient temperature condition on the bottom surface and adiabatic boundary conditions on the four sides. The top surface accounts for convective and radiant losses and evaporation where surfaces temperatures exceed 3042 degrees Celsius. Within the volume of the geometry, temperature dependent material properties are used to calculate heat diffusion and solid-liquid phase change. The incident laser power

distributed by the volumetric heat source, can be modified to vary the predicted melt pool dimensions. By selecting the appropriate heating distribution, the effects of complex and largely unknown physical phenomenon and material properties within the melt pool can be accounted for without being included in the FEA model. The heating distribution is modified by heat source shape and effective absorptivity parameters.

A novel calibration paradigm is employed to select the volumetric heat source parameters which result in the FEA model melt pool predictions that most closely match ground truth measured values. This FEA model and calibration paradigm was described in detail at the 44th International Conference and Expo on Advanced Ceramics and Composites in 2020 [10]. The calibration paradigm employs a set of iterative techniques seeking to minimize the difference between the predicted and target measured melt pool dimensions by modifying the volumetric heat source parameters. The resulting calibrated FEA thermal model predicts a three dimensional transient temperature distribution which aligns the solidus temperature contour spatially with measurements. Shown in Figure 14 are the modeling results and measurement of melt pool width (grey area is temperature >= Ti-6Al-4V solidus temperature). The FEA modeling results are axisymmetric to produce the predicted melt pool width. Temperature predictions from the liquidus contour outward into the far field solid regions are most likely to be accurate; temperatures within the melt pool should be disregarded. Further, the problem is currently under-constrained; the calibrated solutions are not unique which results, most notably, in significant variations in predicted peak temperatures. For purposes of this paper, the solution which best fit target melt pool dimensions with the coolest peak temperature were selected for each track. Future work for this FEA thermal model calibration approach includes targeting the full melt pool contour, rather than only binary dimensions width and depth, as well as incorporating uncertainty quantification and probability. Such future work will address the under-constrained condition of the approach as well as add the capability to account for the high variability in melt pool morphology inherent in metallic additive manufacturing.

The predicted thermal distributions by the model for laser power of 280 Watts and scanning velocities of 500, 850, and 1200 mm/sec are compared to the coaxial NIR measurements as shown in Figure 15 for melt pool width. The thermal model predicts the temperature distribution and is symmetric about the x axis. The coaxial melt pool width is determined

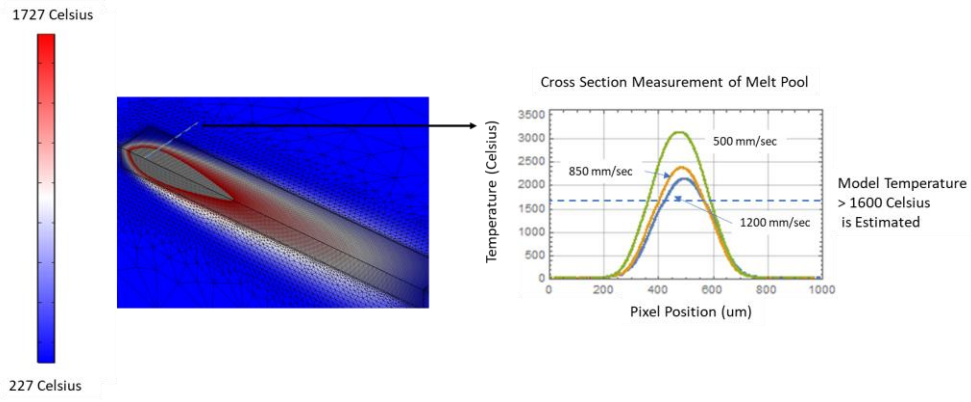

Figure 14: Finite element modeling results of predicted melt pool width.

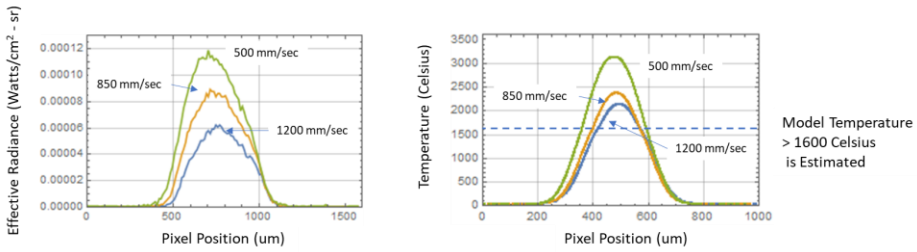

Figure 15: Comparison of finite element modeling results of melt pool width to measured radiance.

from the radiance measurements. Both the model and the coaxial melt pool images were calibrated based on the optical measurements. The coaxial imagery was not converted to temperature for a direct comparison with model temperature since the emissivity varied as shown in Table 1. In addition, the model temperatures above the solidus temperature of 1605 degrees Celsius are only estimated values. The model results as compared to the NIR measurement results show consistency of increasing temperature or radiance as a function of lower laser scan velocities and the general shapes are similar, however the model predicts the heated area outside of the melt pool to be smaller. This could be due to the focus of the laser spot size. Further work to validate the thermal model with the in-situ coaxial thermal measurements will require a more thorough investigation of the input laser power delivered, exact measurement of laser spot size, and better characterization of emissivity. It appears that to remove the emissivity variation will require a pyrometry measurement system using two cameras.

5. CONCLUSIONS

A low cost NIR camera was used in the CAAT system. The infrared camera was radiometrically calibrated to obtain coaxial, inline, imagery of laser generated melt pools. The melt pool imagery was obtained on a bare titanium alloy plate. The surface radiance measurements were compared to optical microscopy images of the melt pool width and an emissivity value was obtained at the melt pool boundary using the solidus temperature value for Ti-6Al-4V. The average emissivity value was 0.20 +/-0.047. This variation is significant and can be due to a number of factors to include geometry effects at the area of laser melting, perhaps reflection of laser detected by the camera, and blurring. One important point to make is without the optical microscopy measurements the melt pool would have been difficult to detect from the camera's radiance imagery. Future work to solve this is to investigate perhaps a pyrometry setup, however the complexity would significantly increase by adding another beam splitter and camera. This will help to determine the melt pool boundary and solidus areas and thus facilitate comparison to the model results.

ACKNOWLEDGEMENTS

This work was done under the NASA's transformational tools and technologies (TTT) additive manufacturing project.

REFERENCES

[1] Yap, C.Y., Chua, C.K., Dong, Z.L., Liu, Z.H., Zhang, D.Q., Loh, L.E., and Sing, S.L., Review of Selective laser melting: Materials and applications, Applied Physics Reviews 2, 041101 (2015); doi:10.1063/1.4935926.

[2] Everton, S., Hirsch, M., Stravroulakis, P., Leach, R., and Clare, A., "A Review of in-situ process monitoring and in-situ metrology for metal additive manufacturing", AI, Materials & Design, vol. 95, April 2016.

[3] Elwarfalli, H., Papazoglou, D., Erdahl, D., Doll, A., and Speltz, J., "In Situ Process Monitoring for Laser-Powder Bed Fusion using Convolutional Neural Networks and Infrared Tomography," 2019 IEEE National Aerospace and Electronics Conference (NAECON), Dayton, OH, USA, 2019, pp. 323-327, doi: 10.1109/NAECON46414.2019.9058251.

[4] Hooper, P.A. Melt pool temperature and cooling rates in laser powder bed fusion. Additive Manufuring 2018, 22, 548–559.

[5] Zalameda, J.N., Burke, E.R., Hafley, R. A., Domack, C. A., Brewer A., and Martin, R.E., "Thermal Imaging for Assessment of Electron-Beam Freeform Fabrication (EBF^3) Additive Manufacturing Deposits", *Proc. SPIE* **2013**, 8705, doi:10.1117/12.2018233.

[6] Solidus Temperature of Ti-6Al-4V,Titanium alpha-beta alloy, Grade 5 (Ti-6Al-4V) [SubsTech], accessed March 2021.

[7] Emissivity of Ti-6Al-4V as a Function of Temperature, TIMETAL_6-4 (spacematdb.com), accessed March 2021.

[8] COMSOL Multiphysics® v. 5.4. www.comsol.com. COMSOL AB, Stockholm, Sweden.

[9] Goldak, John, Aditya Chakravarti, and Malcolm Bibby. "A new finite element model for welding heat sources.", *Metallurgical transactions B* 15.2 (1984): 299-305.

[10] Fody, J., "Developments and Challenges Related to Thermal Process Modeling of Metallic Laser Powder Bed Fusion to Advance Certification of Flight Hardware", presented at 44th International Conference and Expo on Advanced Ceramics and Composites, Daytona, FL (2020, January).